Biomedical Signal Processing and Control 5 (2010) 336–347

Contents lists available at ScienceDirect

Biomedical Signal Processing and Control

journal homepage: www.elsevier.com/locate/bspc

Short communication

On a standing wave Central Pattern Generator and the coherence problem☆

E. Jonckheere[a,*], P. Lohsoonthorn[b], S. Musuvathy[b], V. Mahajan[c,1], M. Stefanovic[d]

[a] Electrical Engineering Dept., University of Southern California, Los Angeles, CA 90089, United States
[b] Electrical Engineering Dept., & Biomedical Engineering Dept., University of Southern California, Los Angeles, CA 90089, United States
[c] Biomedical Engineering Dept., University of Southern California, Los Angeles, CA 90089, United States
[d] Dept. of Electrical and Computer Engineering, University of Wyoming, Laramie, WY 82071, United States

ARTICLE INFO

Article history:
Received 14 April 2009
Received in revised form 14 April 2010
Accepted 22 April 2010
Available online 1 June 2010

Keywords:
Surface Electromyography (sEMG)
Correlation
Wavelets
Central Pattern Generator (CPG)
Sensory-motor loop oscillation
Dural mechanoreceptors
Regeneration in the Central Nervous System (CNS)

ABSTRACT

An electrophysiological phenomenon running up and down the spine, elicited by light pressure contact at very precise points and thereafter taking the external appearance of an undulatory motion of the spine, is analyzed from its standing wave, coherence, and synchronization-at-a-distance properties. This standing spinal wave can be elicited in both normal and quadriplegic subjects, which demonstrates that the neuronal circuitry is embedded in the spine. The latter, along with the inherent rhythmicity of the motion, its wave properties, and the absence of external sensory input once the phenomenon is elicited reveal a Central Pattern Generator (CPG). The major investigative tool is surface electromyographic (sEMG) wavelet signal analysis at various points along the paraspinal muscles. Statistical correlation among the various points is used to establish the standing wave phenomenon on a specific subband of the Daubechies wavelet decomposition of the sEMG signals. More precisely, ∼10 Hz coherent bursts reveal synchronization between sensory-motor loops at a distance larger, and a frequency slower, than those already reported. As a potential therapeutic application, it is shown that partial recovery from spinal cord injury can be assessed by the correlation between the sEMG signals on both sides of the injury.

1. Introduction

Central Pattern Generator (CPG) is a concept still in search of a final definition [13,38]; however, it is admitted that it is an interconnection of neurons that produces a movement of the limbs and/or the trunk that has the following attributes:

1. The movement is rhythmic [50].
2. It does not require (patterned) sensory input [45].
3. The neuronal circuitry in vertebrates is embedded in the spine, without higher cerebral function involvement [26].
4. It requires some learning or entrainment [45] and it might undergo resetting [25].
5. In case of a CPG controlling the movement of the spine of a vertebrate, the latter exhibits some wave properties [13].

Items 1–3 are the most traditional ones, while the consensus is not completely unanimous on Items 4–5. The purpose of this paper is to show evidence of a *human* CPG that produces an undulatory movement of the spine. It satisfies all five criteria, provided Criterion #2, absence of sensory input, is interpreted in a way that *allows* but *does not require* sensory inputs [38], something that will be discussed separately in Section 4.3. In this paper, we more specifically address Criterion #5, since wave properties of CPG movement have lately attracted growing attention [13]. What distinguishes the present paper from [13] is that here we deal with *standing* wave, while [13] dealt with *traveling* wave. We also quite specifically address Criterion #3 by showing that a quadriplegic subject[2] can sustain the undulatory movement. Yet another quadriplegic case study has been reported in [48]. An issue closely related to #3 is whether the CPG is a simple neuronal circuitry, like a bistable oscillator, or something more complicated. For gait CPG, the paradigm of one bistable oscillator CPG per joint [55] seems adequate. Simple bistable oscillators also appear adequate for lower vertebrates (although more complicated models have already been proposed [24]). However, when one reaches the complexity of the human spine, the coordinated movement of its many intervertebral muscles definitely requires a more complicated spatially distributed circuitry.

This rocking motion of the spine, which occurs in the coronal or saggital plane or both depending on the subject, is elicited by light

☆ The research, which involves human subjects, was approved by the Institutional Review Board (IRB) of the University of Southern California and was supported by the Association for Network Care Research Corporation and the Global Gateway Foundation.
* Corresponding author at: 3740 McClintock Avenue, Room EEB 306, Los Angeles, CA 90089-2563, United States. Tel.: +1 213 740 4457; fax: +1 213 821 1109.
E-mail address: jonckhee@usc.edu (E. Jonckheere).
[1] This author is now with Siemens Medical Solutions, India.

[2] Recording on such a vulnerable subject was done with special IRB permission.

1746-8094/$ – see front matter © 2010 Elsevier Ltd. All rights reserved.
doi:10.1016/j.bspc.2010.04.002

pressure contact on the spine at some precise cervical and sacral points. At the cervical level, it is conjectured that the attachment of the spinal dura to the C1–C6 vertebra [4,63] creates a sensory-motor loop oscillation, which is easily visualized as a twitching of the trapezius and sternocleidomastoid neck muscles. (See e.g., [34] for the concept of anatomical loop.) After some entrainment, the skin area overlaying the dural-vertebral attachments is sensitized [54] to the point where a slight pressure contact is enough to elicit the oscillation. The oscillation rapidly becomes self-sustained without the need for further external pressure sensory input from the practitioner. Likewise, at the sacral level, the attachment of the filum terminale (the distal end of the spine) to the coccyx also creates a sensory-motor loop oscillation, which takes the external appearance of a rocking motion of the pelvis. Subject to appropriate entrainment, this pelvic motion can be made to bear some resemblance with human gait. (See [20,11] for the CPG of gait.)

The overall *spinal wave* procedure consists of the following steps: After sensitization of the sacral area, a light pressure contact at S3–S4 engages the sacral oscillator. From the sacral area, an electrophysiological wave phenomenon propagates upward, but initially dissipates before reaching the cervical area. Nevertheless, after some entrainment, eventually the upward wave reaches the cervical area and triggers the neck area to go in oscillation. When extended across the whole spine, the headward traveling wave reflects off the sphenoid, which happens to be the most cephalad attachment of the dura [4], and then travels caudally. Visually, the upward/downward traveling waves can be seen to collide, and survive the collision in some soliton-like propagation [27,22]. Eventually the upward and downward waves settle in a standing wave pattern [1], during which the neck movement is perfectly coordinated with the pelvic movement [28].

It is the latter coordinated movement that has the attributes of a CPG. While the typical CPG features #1, #4, and #5 can be visualized [23], our approach has been to demonstrate the CPG hypothesis by the more objective analysis of the surface electromyographic (sEMG) activity recorded on the paraspinal muscles during the procedure. As such, the rhythmic property was proved in [43] by the burst analysis of the sEMG signals (see also [19] for some closely related research). The learning/entrainment was proved in [30,3] by ARIMA and ACE modeling of the sEMG signals and by showing that the ability of the models to predict the signals improves dramatically along the entrainment. Resetting (e.g., transition from traveling to standing wave) was demonstrated by some qualitative changes in the neck signal models [30].

In this paper, we more specifically demonstrate the standing wave hypothesis #5 by analysis of the sEMG signals recorded at four points (cervical, thoracic, lumbar, and sacral) along the spine [31]. A standing wave across a propagation medium is concurrent with synchronization between the motions of the ends. This synchronization is revealed by a correlation method. The latter further reveals a (s)EMG coherence at ∼10 Hz, a frequency slower than the traditional ∼20 Hz one, because here the coherence is across larger distances [17,49,14,2,16]. Next, we demonstrate that the neuronal circuitry is embedded in the spine (#3) by analyzing the sEMG data recorded on a quadriplegic subject, who, despite a near complete severage of the spine at C5, was able to experience the spinal wave. Finally, the issue of absence of sensory input will also be investigated and a CPG circuitry model will be proposed.

2. Methods

2.1. Data collection

Before data collection, the two research subjects upon which this study is based had signed the *Informed Consent Form* in a protocol approved by the Institutional Review Board (IRB) of the University of Southern California (case USC UPIRB #01-01-009). The control subject is a female in her early 30's and the quadriplegic subject is a male in his 30's. The latter subject had a swimming pool accident: he dove in the end of a pool with 4 ft. of water sustaining a spinal cord injury at C-5 (similar to the case reported in [46]); the C-5 vertebrae was surgically removed and replaced with a titanium plate from C-4 to C-6. Due authorization of the IRB was granted to take recordings on such a vulnerable subject.

To record sEMG signals, we utilized "Uni Patch Tyco EMG Electrodes Round Disk 7500 2.25 diameter Ag snaps." These are ungelled, noninvasive, tripolar electrodes. The patch has 2.25 in. diameter and supports three 0.5 in. Silver disks electrodes arranged at the apexes of an equilateral triangle of 0.75 in. side. Two of the snaps are inputs to a differential amplifier, while the third snap is the ground. The front-end amplifier directly snaps on the patch in order to immediately amplify the signals. The patches were placed at cervical (C2–C3), thoracic (T4–T6), lumbar (L3), and sacral (S2–S4) positions along the spine. The data was recorded with the differential amplifier snaps aligned with the paraspinal muscle fibers [9].

The raw sEMG data was collected over a bandwidth of 10–500 Hz by an Insight^{TM} Millennium machine and the amplified signals (of the order of 2.5 V) were available relative to a ground reference potential. The latter signals were the inputs to a 16 bit precision PC-CARD-DAS16/16, manufactured by *Computer Boards* (now, *Measurement Computing*), configured in "single-ended" mode, and fitting in the PCMCIA slot of a laptop computer. The sampling frequency was 4000 samples/s. It has indeed been argued that it is necessary to sample EMG signals much faster than the Nyquist frequency [47], up to 8000 samples/s; however, a mutual information criterion [48] rather calls for 2000 samples/s. Hence a rate of 4000 samples/s appears a compromise, possibly with some risk of oversampling, which will be removed by the multiresolution wavelet analysis.

In order to assess noise or other irrelevant pattern, before entrainment but with the research subject in the same position and with the same electrode placement and wiring as during entrainment, time-series signals were recorded to be used as control or testing signals. Then, keeping the same experimental environment, the subject was entrained and the spinal wave was recorded. Comparing the wavelet decompositions of the control and the spinal wave signals allowed us to determine which components of the wavelet decomposition were true spinal wave signals as opposed to noise or other parasitic effects.

2.2. Wavelet analysis

Assume we are given a bi-indexed orthonormal family $\{\psi_{mn} : m \in \mathbb{Z}, n \in \mathbb{Z}\}$ of functions, where $\psi_{mn}(t) = 2^{-m/2}\psi(2^{-m}t + n) \in \ell^2$ is obtained by scaling and shifting a "mother function" $\psi \in \ell^2$. This family of functions defines the signal space $\mathcal{Y}$:=span$\{\psi_{mn} : m \in \mathbb{Z}, n \in \mathbb{Z}\}$. As such, any signal $y \in \mathcal{Y}$ can be decomposed as

$$y(k) = \underbrace{\sum_{m>M}\sum_{n} y_{mn}\psi_{mn}(k)}_{A_M(k)} + \underbrace{\sum_{m\le M}\sum_{n} y_{mn}\psi_{mn}(k)}_{\sum_{m\le M} D_m(k)}$$

where the y_{mn}'s are the coefficients of the expansion of the signal in the bi-indexed wavelet basis. $\sum_{m>M}\sum_n y_{mn}\psi_{mn}$ can be interpreted as the (low resolution) *approximation* of the signal, while $\sum_{m\le M}\sum_n y_{mn}\psi_{mn}$ is the (high resolution) *detail* of the signal.

If we define $V_M = \text{span}\{\psi_{mn} : m > M, n \in \mathbb{Z}\}$, we obtain a sequence of signal approximation spaces $\cdots \subset V_{m+1} \subset V_m \subset$

$V_{m-1} \subset \cdots$ Furthermore, we write $V_{m-1} = V_m \oplus W_m$, where $W_m = \text{span}\{\psi_{mn} : n \in \mathbb{Z}\}$. It turns out that there exists a scaling function ϕ such that $V_m = \text{span}\{\phi_{mn} : n \in \mathbb{Z}\}$, $\phi_{mn}(t) = 2^{-m/2}\phi(2^{-m}t + n)$. This function is computed via a wandering subspace argument [37]. Define the "outgoing" subspace $V_{0+} = \text{span}\{\psi_{mn} : m > 0, n \in \mathbb{N}\}$ and the positive shift $T_+ : V_{0+} \to V_{0+}, (T_+\psi)(k) = \psi(k+1)$. Then clearly, $T_+V_{0+} \subset V_{0+}$ and we pick $\phi \in V_{0+} \ominus T_+V_{0+}$ (see [39, Section 5, Proposition 5]).

With the above defined subspaces, and taking $M = 1$ as reference resolution level, the signal can be dyadic decomposed down to eight levels as

$$\begin{aligned}
Y(k) &= \sum_n c_{1n}\phi_{1n}(k) + \sum_{m\le 1}\sum_n c_{mn}\psi_{mn}(k)\\
Y(k) &= \sum_n c_{2n}\phi_{2n}(k) + \sum_n c_{2n}\psi_{2n}(k) + \sum_{m\le 1}\sum_n c_{mn}\psi_{mn}(k)\\
&\vdots \qquad\qquad \vdots\\
Y(k) &= \sum_n c_{8n}\phi_{8n}(k) + \sum_n c_{8n}\psi_{8n}(k) + \sum_n c_{7n}\psi_{7n}(k)\\
&\quad + \cdots + \sum_n c_{2n}\psi_{2n}(k) + \sum_{m\le 1}\sum_n c_{mn}\psi_{mn}(k)
\end{aligned}$$

For the specific case $y \in V_0$, the above is rewritten more conceptually in terms of various approximation (A) and detail (D) components:

$$\begin{aligned}
Y(k) &= A_1(k) + D_1(k)\\
Y(k) &= A_2(k) + D_2(k) + D_1(k)\\
&\vdots \qquad \vdots\\
Y(k) &= A_8(k) + D_8(k) + D_7(k) + \cdots + D_1(k)
\end{aligned}$$

The experimental problem is to determine *what* wavelet and *what* subband signals among the $D's$ are most relevant to the spinal wave.

2.3. Correlation approach to wave analysis

The wave analysis proceeds from the correlation properties of the signal recorded at one point along the spine and the time-shifted signal recorded at another point (see [40] for a related analysis). Here the sEMG signals recorded at two points along the spine are treated as stationary random processes $Y_i(k)$, $Y_j(k)$. (The stationary assumption is approximately verified over a small enough time window [43].) The scalar correlation coefficient [5, p. 74] between the random variables $Y_i(k)$ and $Y_j(k+s)$ is defined as

$$\rho_{ij}(s) = \frac{E((Y_i(k) - EY_i(k))(Y_j(k+s) - EY_j(k+s)))}{\sqrt{E(Y_i(k) - EY_i(k))^2}\sqrt{E(Y_j(k+s) - EY_j(k+s))^2}}$$

This approach is statistically implemented as follows [5, Chap. 12]:

$$r_{ij}(s) = \frac{\sum_{k=1}^{K-s}(Y_i(k) - \bar{Y}_i(s))(Y_j(k+s) - \bar{Y}_j(s))}{\sqrt{\sum_{k=1}^{K-s}(Y_i(k) - \bar{Y}_i(s))^2}\sqrt{\sum_{k=s+1}^{K}(Y_j(k) - \bar{Y}_j(s))^2}}$$

where

$$\bar{Y}_i(s) = \frac{1}{K-s}\sum_{k=1}^{K-s} Y_i(k)$$

$$\bar{Y}_j(s) = \frac{1}{K-s}\sum_{k=s+1}^{K} Y_j(k)$$

Given that $r_{ij}(s) \neq 0$, it is necessary to determine, with enough confidence, whether $\rho_{ij}(s) \neq 0$. This confidence analysis is based on the fact that, when $Y_i(k)$, $Y_j(k+s)$ are independently normally distributed ($\rho_{ij} = 0$), the variable

$$t_{ij} = r_{ij}\frac{\sqrt{K-s-2}}{\sqrt{1-r_{ij}^2}}$$

approximately follows a t-distribution with $K - s - 2$ degrees of freedom [5, p. 224], where K is the length of the data record and s the time shift.[3] To compute the $(100 - 2\alpha)\%$ confidence interval, define t_α to be the value of the t-variable that is exceeded with probability α. Then the confidence interval is given by $[-r, +r]$, where r is the solution to $t_\alpha = r\left(\sqrt{K-s-2}/\sqrt{1-r^2}\right)$, that is,

$$r \approx \frac{t_\alpha}{\sqrt{K-s-2}} \tag{1}$$

3. Results

3.1. Wavelet decomposition

The initial intent was to find a specific wavelet and the specific subband signals that could achieve the most sizable distinction between some "test" signals and the spinal wave signals. Here, "test" means that the sEMG data was recorded during some voluntarily controlled mild motion of the trunk. Another criterion was to find the subband signals that exhibit best correlation (hence highest confidence). After trial and error, it was found that the Daubechies DB3 wavelet [8,61,7] was the best suited relative to the above-mentioned criteria.

In Fig. 2, a "test" signal segment and the first half of the raw spinal wave signal as shown in Fig. 1, are dyadic decomposed down to 8 levels with the Daubechies wavelet function [8,61,7] of order 3. These two segments, both of a length of approximately 2.5 s, were chosen as "most relevant" within the sEMG database of the control subject in a sense elaborated on in [30, Section 2.3]. In a few words, the whole control subject data record was subdivided in some smaller "segments." Each segment was represented by the sum of the absolute values of its partial correlation coefficients b_k and the sum of the absolute values of its autocorrelation coefficients a_k. Then the relevant data $\left\{\left(\sum_{k=1}^{25}|a_k|, \sum_{k=1}^{25}|b_k|\right)\right\}$ was displayed as a cluster in $\mathbb{R}^2$. Then the "most relevant" signal segment was defined as the center of mass of the cluster. The raw signals of Fig. 2 were obtained as the most relevant ones.

By comparing the "test" and spinal wave signals, it becomes evident that the signals in A_8 are just base line drifting or low frequency noises (long term evolution) and as such are signals of no interest; neither are the signals in the D_1 to D_5 subbands of interest, because there is no difference between the test and the spinal wave signals and as such these signals consist mainly of high frequency noise. On the other hand, the D_6, D_7, D_8 components are of more interest, because there is now a sizable difference between

[3] Also recall that the sample distribution of $(1/2)\log((1+r)/(1-r))$ is approximately normal with mean $(1/2)\log((1+\rho)/(1-\rho))$.

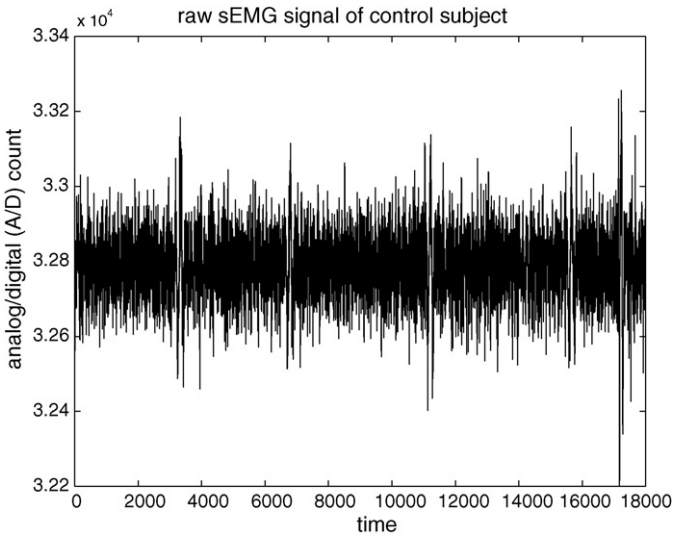

Fig. 1. Raw sEMG signal of control subject. The abscissa is the number of samples at a rate of 4000/s; the ordinate is the analog/digital (A/D) count among the 2^{16} available in the 16-bit precision analog-to-digital converter.

the test and spinal wave signals. "Wavelet packets" can be observed in the D_7, D_8 subband signals, which, as will be shown, are coherent bursting phenomena [17,16] running up and down the spine and establishing a "standing" wave pattern. Quantitatively, looking at the D_8 subband signal, it appears that the bursts occur at a rate of 1 every 4000 samples, that is, at a rate of 1 burst per second, which is consistent with the visually observed motion of the spine. Zooming at a burst of the D_8 subband signal, it is easily seen that it is composed of several cycles of a more fundamental oscillation, at a frequency of roughly 13.5 Hz.

While a correlation analysis on D_7 could be carried out, we selected the D_8 signal, because it showed the better correlation properties. Another motivation for focusing on the D_8 (and possibly the D_7) subband signals is that comparison between Fig. 1 and Fig. 2, right panel, reveals that the mild bursts in the raw signal occur when the D_8 (D_7) subband signals show doublets.

Observe that Fig. 2 only provides a 2.5 s snapshot of the wavelet decomposition, whereas the correlation analysis is based on a much longer data records: 1 min and 20 s for control subject and 50 s for quadriplegic subject.

3.2. Correlation plots

The correlation plots $r_{ij}(s)$ for various time-shifts of the D_8 subband signals of the control (normal) subject are shown in Figs. 3(a)–6(a).

The confidence level was set to 99%. The confidence intervals were computed from Formula (1), with $\alpha = 0.005$, $t_{0.005} = 2.576$ (for the Gauss approximation of very high degree of freedom t-distribution), $s = 0$, and $K = 327,680$ for control subject and $K = 196,608$ for quadriplegic subject. The resulting confidence intervals are $[-0.0045, +0.0045]$ for control subject and $[-0.0058, +0.0058]$ for quadriplegic subject. They are displayed by two lines parallel to the s-axis in Figs. 3–6. The correlation is significant whenever the $r_{ij}(s)$ versus s curve is outside the horizontal band bounded by the two lines parallel to the s axis.

Observe that the curves are well outside the "slit" along the s axis, indicating a 99% confidence in the correlation. Next, observe that all correlations are maximum for $s = 0$; in other words, the cervical, thoracic, lumbar and sacral bursts are synchronous, a first sign of a standing wave pattern. Most importantly, observe the consistent phase pattern, with "zero correlation nodes." (A "zero correlation node" is defined as a point where all $r_{ij}(s)$ versus s curves cross the $r = 0$ axis.) Also observe that the two successive maxima of $r_{11}(s)$ occur for $\Delta s \approx 275$ samples ≈ 0.06875 s, which is consistent with the fundamental frequency of 13.5 Hz. observed in Section 3.1.

To allow for an easy comparison between the control and quadriplegic subjects, the correlation curves of Figs. 3(a)–6(b) are organized with the control subject curves on the left and

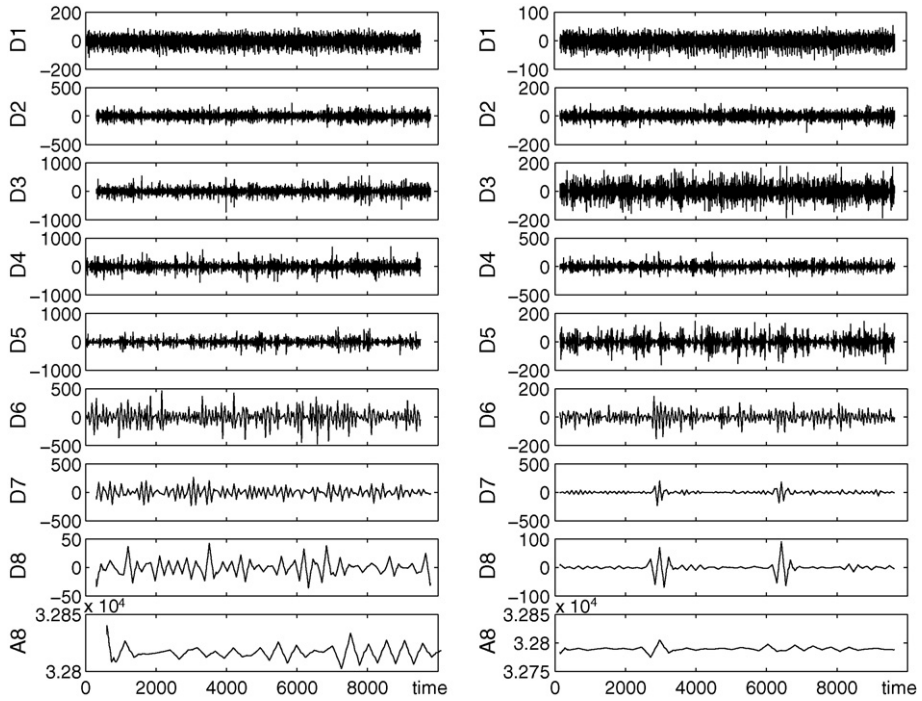

Fig. 2. Comparison between wavelet decompositions of test signal (left) and spinal wave signal (right). The sampling rate is 4000/s. The raw spinal wave signal is the first half of the signal shown in Fig. 1.

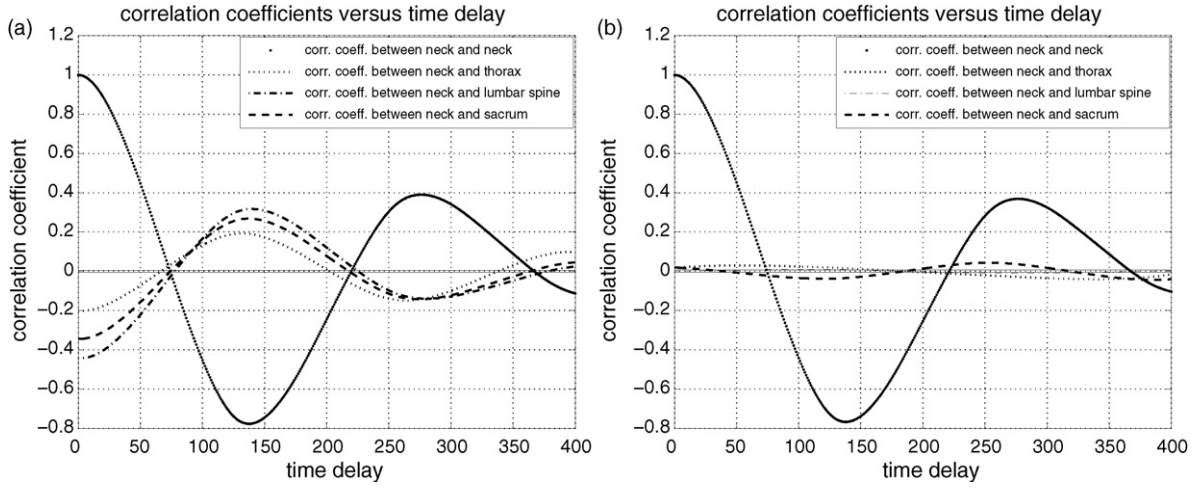

Fig. 3. (a and b) Correlation between D_8 subbands of neck and other signals for control subject and quadriplegic subject. Solid line: neck–neck correlation; dotted line: neck–thorax correlation; dashed-dotted line: neck–lumbar spine correlation; dashed line: neck–sacrum correlation. Confidence interval for control subject: [−0.0045, +0045]; for quadriplegic subject: [−0.0058, +0.0058].

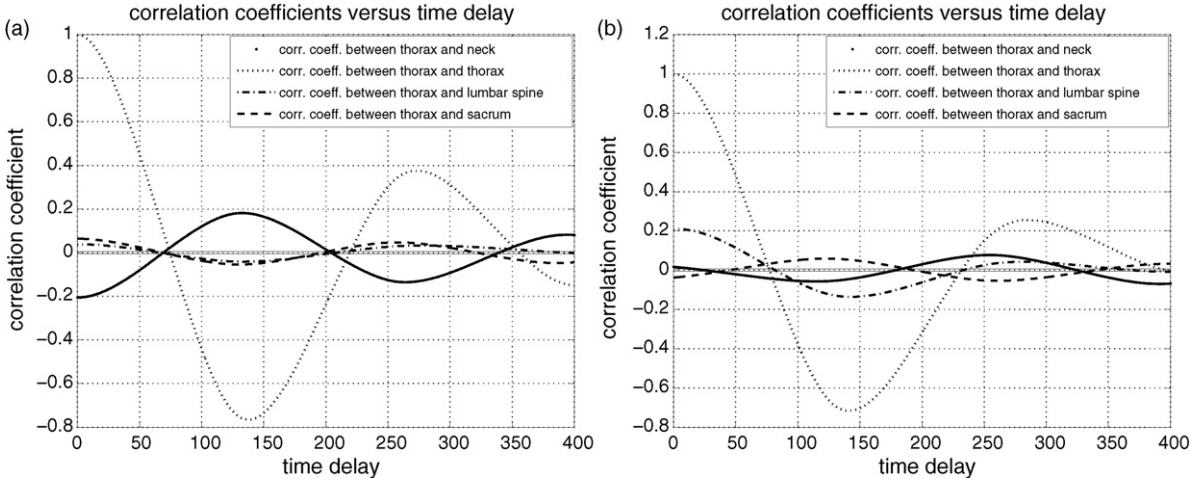

Fig. 4. (a and b) Correlation between D_8 subbands of thorax and other signals for control subject and quadriplegic subject. Solid line: thorax–neck correlation; dotted line: thorax–thorax correlation; dashed-dotted line: thorax–lumbar spine correlation; dashed line: thorax–sacrum correlation. Confidence interval for control subject: [−0.0045, +0045]; for quadriplegic subject: [−0.0058, +0.0058].

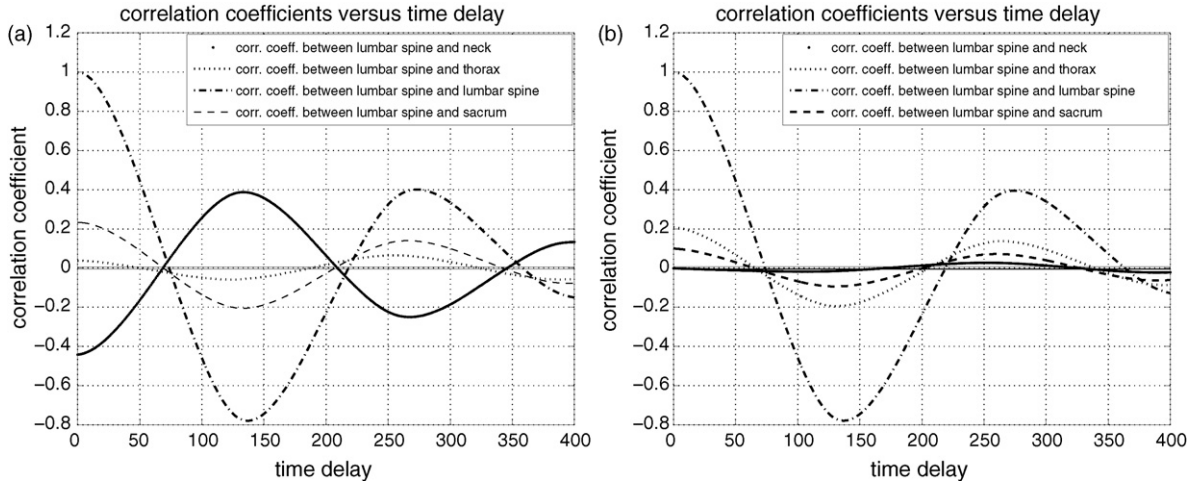

Fig. 5. (a and b) Correlation between D_8 subbands of lumbar spine and other signals for control subject and quadriplegic subject. Solid line: lumbar spine–neck correlation; dotted line: lumbar spine–thorax correlation; dashed-dotted line: lumbar spine–lumbar spine correlation; dashed line: lumbar spine–sacrum correlation. Confidence interval for control subject: [−0.0045, +0045]; for quadriplegic subject: [−0.0058, +0.0058].

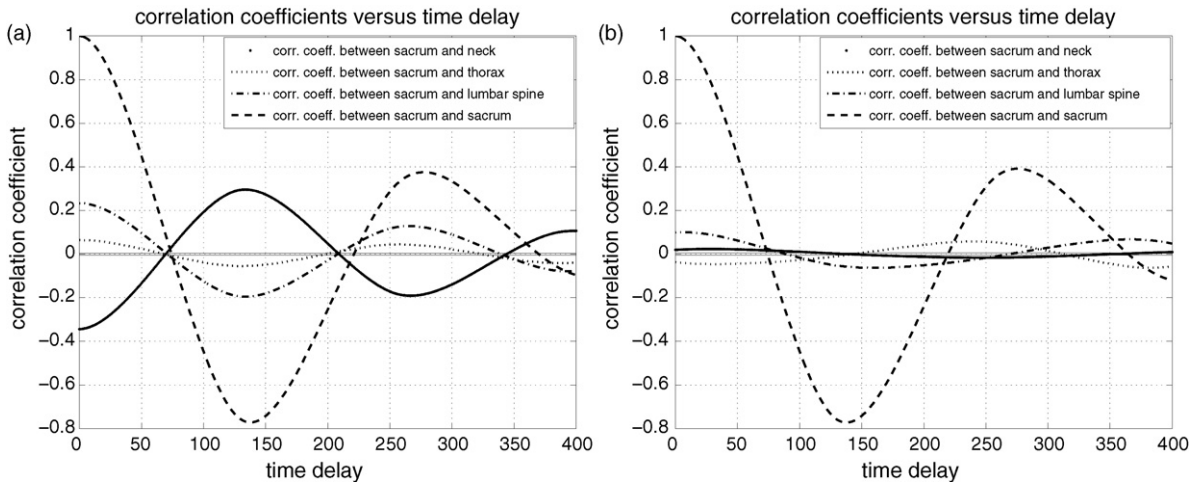

Fig. 6. (a and b) Correlation between D_8 subbands of sacrum and other signals for control subject and quadriplegic subject. Solid line: sacrum–neck correlation; dotted line: sacrum–thorax correlation; dashed-dotted line: sacrum–lumbar spine correlation; dashed line: sacrum–sacrum correlation. Confidence interval for control subject: [−0.0045, +0045]; for quadriplegic subject: [−0.0058, +0.0058].

the quadriplegic subject curves on the right. The first and most striking difference between the control subject (Fig 3(a)) and the quadriplegic subject (Fig 3(b)) is a weaker correlation between, on the one hand, the neck and, on the other hand, the cervical, thoracic, lumbar or sacral signals, as can be anticipated because of the neck injury. However, no matter how weakened, the correlations involving the neck *are still in the 99% confidence interval.* Second, observe that the pattern of "zero crossing nodes" is not as clear as that of the control subject. However, the thoracic, lumbar, and sacral plots (Figs. 4(b), 5(b), and 6(b), respectively) do show zero crossing nodes, *if we remove the neck signals from those plots.* Another striking difference is that, in the thoracic, lumbar and sacral plots of Figs. 3(a)–6(b), the correlation involving the neck signal of the quadriplegic subject is off phase as compared with the control subject.

3.3. Comparison with other case studies

Among the two dozens case studies we have conducted, the present control subject case is among the best we have analyzed from the point of view of zero correlation crossing pattern. (The very best case is one that does not even require preprocessing of the data by wavelet transform, as the zero correlation crossing pattern already appears on the raw signal.) Among the cases that require wavelet transform pre-filtering, the present control case study stands out as a nice one in the sense that (i) the neck–neck correlation curve crosses the time delay axis at the same points where the other correlation curves cross the same axis, and (ii) the zero crossing nodes appear all along the time delay axis. In some cases, there are difficulties at either (i) getting the neck–neck curve crossing the time delay axis at the right places, or (ii) having the zero crossing node pattern already present at small time delays.

4. Discussion

4.1. Wavelet decomposition

The finding that the DB3 wavelet is the best relative to the criteria of Section 3.1 is fully consistent with [60], where DB_3 was also adopted, for the different reason that this wavelet mimics the single Motor Unit Action Potential (MUAP) detected by the electrodes. This explains the experimentally observed fact that the DB3 subband signals have better correlation properties. The nice D_8 subband signal reveals that the muscle fibers and hence efferent nerve fibers [58, p. 66] are in sync; indeed, there is evidence that the sEMG signal is the algebraic summation of motor-unit action-potential trains [10,44].

The bursts are easily seen to occur at a rate of approximately one per second, which is consistent with the observable mechanical motion of the spine. The bursts appear to be doublets [14,2,32], which from the point of view of the classification of [49, Fig. 1] are of the "resonant" type. The in-burst frequency of ∼13.5 Hz appears closely related to a ∼10 Hz phenomenon conjectured to exist in EMG [17, the question of frequency], but this issue is relegated to Section 4.2.5.

4.2. Standing wave interpretation of correlation

4.2.1. Mathematical modeling: general function analytic analysis

Let the space-sampled, time-sample signal $(y_{\text{neck}}(k), y_{\text{thorax}}(k), y_{\text{lumbar}}(k), y_{\text{sacrum}}(k))$ be smoothly extended as a function of the continuous variables $x \in [0, L]$ and $t \in [0, T]$. x is the position along the spine, L is the length of the spine, t is the time, and T is the length of the data record. By fundamental bandwidth limitation, $y(x, t)$ is continuous, it is furthermore bounded by the saturation of the amplifiers, so that the Hilbert-Schmidt condition $\int_0^L \int_0^T y^2(x,t)\,dx\,dt < \infty$ holds. Hence the data $y(x, t)$ can be viewed as the kernel of an integral operator $Y : L^2[0, T] \to L^2[0, L]$ of the Hilbert-Schmidt type [12, p. 1009], where $L^2[0, T]$ denotes the classical Lebesgue space of functions square integrable over $[0, T]$.

Form the adjoint $Y^* : L^2[0, L] \to L^2[0, T]$ along with the self-adjoint operator

$$\begin{pmatrix} 0 & Y^* \\ Y & 0 \end{pmatrix} : L^2[0,T] \oplus L^2[0,L] \to L^2[0,T] \oplus L^2[0,L]$$

This operator is also clearly Hilbert-Schmidt, hence compact. It is furthermore nonsingular if it is assumed that Y is nonsingular. It is also easily seen that its eigenvalues come in opposite pairs. Write the eigenvector equation

$$\begin{pmatrix} 0 & Y^* \\ Y & 0 \end{pmatrix} \begin{pmatrix} f_n \\ \pm g_n \end{pmatrix} = \pm\sigma_n \begin{pmatrix} f_n \\ \pm g_n \end{pmatrix}, \quad n \in \mathbb{N}^*$$

where $\sigma_n > 0$, $\sum_n \sigma_n^2 < \infty$ (as a corollary of the Hilbert-Schmidt property [12], Th. XI.6.25), and $\{f_n\}$, $\{g_n\}$ are orthonormal systems. Then applying Mercer's theorem [12, p. 1088] to the projections of

$\begin{pmatrix} 0 & Y^* \\ Y & 0 \end{pmatrix}$ on its positive and negative spectra yields

$$y(x,t) = \sum_{n\in\mathbb{N}^*} \sigma_n f_n(t) g_n(x)$$

where the convergence is to be interpreted in the sense of the Hilbert-Schmidt norm [12, Th. XI.6.4]. (See [51] for the formalization of Mercer's theorem extended to non sign definite operators.)

Before proceeding further, some lemmas are needed; the proofs are relegated to Appendix A.

Lemma 1. *The functions $f_n : [0,T] \to \mathbb{R}$ and $g_n : [0,L] \to \mathbb{R}$ are continuous.*

Observe that the continuity of g does not preclude $g_n(0) = \infty$ or $g_n(L) = \infty$. However, the boundedness of $y(x,t)$ does preclude this to happen. So, g_n is bounded, but not uniformly in n.

Next, form

$$\overline{f_n(t) f_m(t+s)} := \frac{1}{T}\int_0^T f_n(t) f_m(t+s)\,\mathrm{d}t$$

It is readily observed that the above is continuous and uniformly bounded in s; specifically, $\left|\overline{f_n(t) f_m(t+s)}\right| \le 1/T$, as a consequence of the Cauchy-Schwarz inequality.

Now, we construct the crucial mathematical object: the correlation between the signal at one spatial point x and the time shifted signal at another spatial location x':

$$R_{x,x'}(s) := \overline{y(x,t) y(x',t+s)}$$

From its definition, it is easily seen that $R_{x,x'}(s) : [0,L]^2 \times [0,T] \to \mathbb{R}$ is continuous and bounded. Next, we would like to show that in the above $y(x,t)$ can be replaced by its Mercer-like expansion. But another lemma is needed.

Lemma 2. *The trace class property $\sum_{n=1}^{\infty} \sigma_n < \infty$ holds.*

Now, we are in a position to formulate a property of the spatio-temporal correlation that will appear crucial in the sequel; the proof of it is relegated to Appendix A.

Theorem 1.

$$R_{x,x'}(s) = \sum_{n,m=1}^{\infty} \sigma_n \sigma_m \overline{f_n(t) f_m(t+s)} g_n(x) g_m(x')$$

and the convergence is in the Hilbert-Schmidt norm.

From the various plots of $R_{x,x'}(s)$ for the control subject and *continuity* of the correlation, it is clear that, $\forall x$, there exists a x^* such that

$$R_{x,x^*}(s) = \sum_{n,m=1}^{\infty} \sigma_n \sigma_m \overline{f_n(t) f_m(t+s)} g_n(x) g_m(x^*) = 0, \forall s$$

In particular, the above is true for $s = 0$ and upon integration relative to t, it is found that

$$\sum_n \sigma_n^2 g_n(x) g_n(x^*) = 0$$

In view of the orthogonality of $\{g_n\}$, the above yields

$$g_n(x^*) = 0, \forall n$$

It follows that $y(x^*,t) = 0, \forall t$, so that x^* is a *mode shape node*, indicative of a *standing wave*.

4.2.2. Mathematical modeling: harmonic analysis

From the correlation plots, the cervical ($x = 0$) and sacral ($x = L$) activities of the control subject are easily seen to be in opposite phase. (This is an example of *synchronization across a significant distance* [35, Fig. 2].) This opposite phase phenomenon at the end points along with the standing wave property justifies an approximate model of the form:

$$y(x,t) = \sum_{n=1}^{\infty} a_n \sin(n\omega t) \cos\left(\frac{(2n-1)kx}{2}\right) \tag{2}$$

where $k = 2\pi/L$ is the wave number and L is the length of the propagation medium. In this model, the mode shape node is located at $x^* = L/2$, which is consistent with the experimentally observed *muscle activity* node between the neck and the thorax. This simple harmonic model is useful to clarify the fundamental frequencies involved in this phenomenon.

With such a model, the correlation is easily obtained as

$$R_{x_1,x_2}(s) := \overline{y(x_1,t) y(x_2,t+s)} = \sum_{n=1}^{\infty} a_n^2 \cos(n\omega s) \cos\left(\frac{2n-1}{2} k x_1\right) \times \cos\left(\frac{2n-1}{2} k x_2\right)$$

The zero correlation nodes reveal that $R_{x_1,x_2}(s^*) = 0, \forall x_1, x_2$. From

$$\int_0^L \int_0^L R_{x_1,x_2}(s^*) \cos\left(\frac{2N_1-1}{2} k x_1\right) \cos\left(\frac{2N_2-1}{2} k x_2\right) \mathrm{d}x_1\, \mathrm{d}x_2 = 0$$

it follows that $\cos N\omega s^* = 0, \forall N$, so that $s^* = (2m - 1/2N)(\pi/\omega)$. To be consistent with the experimentally observed pattern of s^*, the expansion can only contain one term $n = 1$. As such the pattern $\{s^* = (2m - 1/2)(\pi/\omega) : m \in \mathbb{N}^*\}$ is remarkably consistent with the zero correlation pattern of the figures. Pursuing further, the first ($m = 1$) zero correlation node occurs at $s^* = 80$ samples points, that is, $s^* = 80/4000$ s. Hence $\omega = (1/2)(\pi/s^*)$ yields a frequency of 12.5 Hz.

It is interesting to observe that the Step 2 of the algorithm of [13] also involves truncation of an infinite series like (2), so that our analysis provides the justification for this truncation.

4.2.3. Mathematical modeling: wavelet analysis

Let ψ be the (continuous time) DB3 mother function and let $\{\psi_{8,n}(t) = 2^{-4}\psi(2^{-8}t + n) : n \in \mathbb{Z}\}$ be the orthonormal basis of the D_8 space [7], where n is the shift. Here an analysis similar to that of the preceding paragraph is developed, except for a wavelet instead of a sine time dependence:

$$y_8(x,t) = \sum_n g_{8,n}(x) \psi_{8,n}(t) \tag{3}$$

where the $g_{8,n}$'s are the mode shapes. In this wavelet setup, the correlation becomes

$$\begin{aligned} R_{x_1,x_2}(s) &:= \overline{y_8(x_1,t) y_8(x_2,t+s)} \\ &= \sum_{n_1}\sum_{n_2} g_{8,n_1}(x_1) g_{8,n_2}(x_2) \overline{\psi_{8,n_1}(t)\psi_{8,n_2}(t+s)} \\ &= \sum_{n_1} g_{8,n_1}(x_1) g_{8,n_1-2^{-8}s}(x_2) \end{aligned}$$

Therefore, the zero correlation nodes are given by the s-solutions to

$$\sum_{n_1} g_{8,n_1}(x_1) g_{8,n_1-2^{-8}s}(x_2) = 0, \forall x_1, x_2$$

From the structure of the plots, such solutions appear in a pattern with period 2^8.

Next, setting $s = 0$ in the preceding yields

$$R_{x_1,x_2}(0) = \sum_{n_1} g_{8,n_1}(x_1) g_{8,n_1}(x_2)$$

If we set $i = 1, 2, 3$,and4 for the neck, thorax, lumbar spine, and sacrum, respectively, the matrix of canonical correlations $\{r_{x,x_j}(0)\}_{i,j=1,\ldots,4} := \{(R_{x_i,x_j}(0))/(R^{1/2}_{x_i,x_i}(0) R^{1/2}_{x_j,x_j}(0))\}_{i,j=1,\ldots,4}$ is obtained numerically as $\begin{pmatrix} 1.0000 & -0.2000 & -0.4400 & -0.3400 \\ -0.2000 & 1.0000 & 0.0300 & 0.0600 \\ -0.4300 & 0.0300 & 1.0000 & 0.2400 \\ -0.3400 & 0.0600 & 0.2600 & 1.0000 \end{pmatrix}$. It is symmetric, up to rounding error, as expected, but most importantly, observe the change of sign in the correlation from the neck to the thorax. Hence there exists a point $x^* \in (x_1, x_2)$ such that $r_{x_1,x^*}(0) = 0$ and furthermore from the shape of the plots $r_{x_1,x^*}(s) = 0$, $\forall s$. It follows that

$$\sum_{n_2} g_{8,n_2+2^{-8}s}(x_1) g_{8,n_2}(x^*) = 0$$

Since $g_{8,n_2+2^{-8}s}(x_1) \neq 0$ because of the neck activity, we get $g_{8,n_2}(x^*) = 0$. The latter indicates existence of a *mode shape node* at x^*. Clearly, there exists such a node somewhere along the nervous pathway between the neck electrode and the thoracic electrode. Besides, at the skeletomuscular level, such a mode shape node can be directly observed during the spinal wave motion [23].

4.2.4. Standing wave versus coherence

Here, the *standing wave* pattern between the various signals has been derived from the *zero crossing nodes* of the *time-domain* correlation:

$$\rho_{ij}(s) = \frac{E(Y_i(t) Y_j(t+s))}{(EY_i^2(t))^{1/2} (EY_j^2(t))^{1/2}} \tag{4}$$

On the other hand, Farmer [17,16] defines the frequency-dependent *coherence* between two signals Y_i, Y_j as *peaks* in the *frequency-domain* correlation plot[4]:

$$\hat{\rho}_{ij}(\jmath\omega) = \frac{|S_{ij}(\jmath\omega)|}{(S_{ii}(\jmath\omega))^{1/2} (S_{jj}(\jmath\omega))^{1/2}} \tag{5}$$

where $S_{k\ell}(\jmath\omega)$ is the (cross)spectral density, that is, the Fourier transform of $E(Y_k(t) Y_\ell(t+s))$ relative to s.

The relationship between the time-domain and frequency-domain concepts is a bit tenuous:

$$\rho_{ij}(0) = \frac{\int_{-\infty}^{+\infty} S_{ij}(\jmath\omega)\, \mathrm{d}\omega}{\left(\int_{-\infty}^{+\infty} S_{ii}(\jmath\omega)\, \mathrm{d}\omega\right)^{1/2} \left(\int_{-\infty}^{+\infty} S_{jj}(\jmath\omega)\, \mathrm{d}\omega\right)^{1/2}} \overset{???}{\approx} \frac{S_{ij}(\jmath\omega)}{S_{ii}^{1/2}(\jmath\omega) S_{jj}^{1/2}(\jmath\omega)}$$

Besides, under a time shift in one of the signals $Y_j(t) \to Y_j(t + \Delta T)$, $\hat{\rho}_{ij}(\jmath\omega)$ remains unchanged, while $\rho_{ij}(s)$ would be changed and the zero crossing node pattern would be shattered. Therefore, the standing wave pattern as revealed by the "zero crossing nodes" is a property stronger than the "coherence," but the neurophysiological phenomena that both techniques attempt to pin down are unmistakenly the same.

[4] See Matlab Signal Processing toolbox function `mscohere`.

4.2.5. Bursts: coherence and the questions of frequency and phase

To summarize, the D_8 bursts occur synchronously at the neck, thorax, lumbar spine, and sacrum. Thus the bursts occur in a standing wave pattern. Next, the in-burst oscillations in the thoracic, lumbar, and sacral areas are in phase, and in opposite phase relative to the in-burst oscillations at the cervical level. Thus there is also a standing wave pattern within each D_8 burst and the in-burst oscillations encode the movement phase information.

A 180° phase locking phenomenon, similar to the one observed between the cervical and the thoracic to sacral levels but for EEG-EMG coherence, has also been reported in [21, p. 6].

EMG coherence across the ∼2 cm distance between the adductor pollicis (AdP) and the first dorsal interosseous (1DI) has been observed at ∼25 Hz [17, Fig. 5(G)], [16, Fig. 2(D)] as the peak of $\hat{\rho}_{\mathrm{AdP,1DI}}(\jmath\omega)$. Here, the slower frequency of ∼12.5–13.5 Hz is observed across significantly larger (∼1m) distances. Also observe that our coherence of about ∼0.3 is larger than the ∼0.24 observed in [17, Fig. 5(G)], especially since the former was observed across substantially longer distances.

4.2.6. Standing wave: control versus quadriplegic subject

The cervical electrode was positioned at C2–C3 on the upper trapezius, which is innervated by C2–C3. The sacral electrode was positioned at S2–S4 on the latissimus, which is innervated by C6–C8. Since the injury was at C5, the correlations r_{14}, r_{41} provide a measure of the correlation of the innervation signals on both sides of the spinal cord injury. The fact that $r_{14}, r_{41} > 0$, as shown by Fig. 3,6, indicates that nerve impulses pass through, or peripherally around, the injury area, consistently with the partial motor recovery.

Second, the standing wave pattern does not appear as clearly as for the control subject, as can be seen from the defective "zero correlation nodes." Nevertheless, it appears that there is some standing pattern involving the thorax, lumbar spine, and sacrum, but not involving the neck. Again, this is fully consistent with the C5 injury.

The abnormal synchronization observed on the quadriplegic subject is consistent with a similar observation made in [17, Fig. 3]): the loss of coherence between two single motor units of the first dorsal interosseus (1DI) of a subject who had suffered a infarct of the right internal capsule. Along the same line, in [17, the question of frequency], the lack of Magnetoencephalographic-EMG coherence at ∼10 Hz led to the conjecture that the "*slow movement* ∼10 Hz *drive may not be expressed at the level of the motor cortex*" but may involve the somatosensory cortex and the cerebellum. The fact that the quadriplegic subject had deficient ∼10 Hz coherence provides some evidence in favor of this last conjecture. Ref. [33] points to the severage of the *sensory pathway* as more specifically responsible for the deficient coherence. Clinical results on another quadriplegic subject have recently been collected [15,48], with the major result that the cervical oscillator is chaotic while the sacral oscillator is not, with of course the impossibility to have coherence between a chaotic and a nonchaotic motion.

4.3. Absence of sensory input

It is usually admitted that a CPG does not necessitate sensory input to produce a rhythmic motion, except during entrainment and resetting [13,45]. Here, during entrainment, the CPG certainly uses sensory input from the mechanoreceptors. After entrainment, the spinal wave becomes self-sustained without practitioner's *external* pressure input. The extent of the involvement of the sensory-motor loop in the self-sustained spinal wave phenomenon is unclear at this stage, but our conjecture is that some sensory input is still generated, probably not as significantly as during entrainment/resetting. The situation would be a bit like the lamprey experiment [45], where the mechanoreceptors send some

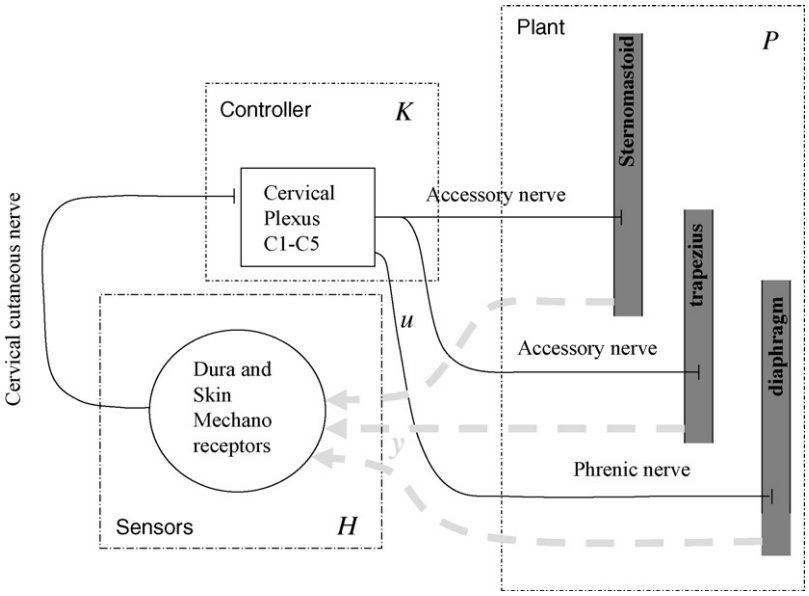

Fig. 7. Sensory-motor loop at cervical level. The hard lines are established pathways, whereas the dotted lines are the conjectured paths through which the loop closes. This diagram is drawn using control conventions: *K* is the controller, *u* is the control action, *P* is the plant, and *H* is the sensor array.

internal sensory input to the spine [41], and an anatomical loop closes.

The fact that a CPG does not necessitate sensory input to sustain a rhythmic motion does not, however, preclude some sensory input to "*modulate*" the CPG [56]. This is, we believe, what happens here: the CPG is modulated by the neck and sacrum oscillators to go in a standing wave pattern. In [38], it is argued that the combination of a feedforward CPG oscillator and sensory feedback is the best strategy to secure proper functioning in case of poor sensory feedback and external disturbances. The quadriplegic subject case produces such an example: our best assessment is that the burst fracture was at the place of, or below, the dural-vertebral attachment, so that the neck sensory information was severely distorted, or simply unavailable, resulting in a partial loss of the standing wave property, yet the spinal wave phenomenon was still present.

5. Further discussion: anatomical loops and CPG circuitry model

5.1. Biological oscillators

The cervical and sacral anatomical loops are shown in Figs. 7 and 8. In both of them, it is conjectured that the loop closes via the mechanoreceptors, which pick up muscle activity and send proprioceptive signals to some specific plexus of the cord. Even though mechanoreceptors are distributed all along the lateral portion of the human spine [57], it does not appear possible to elicit

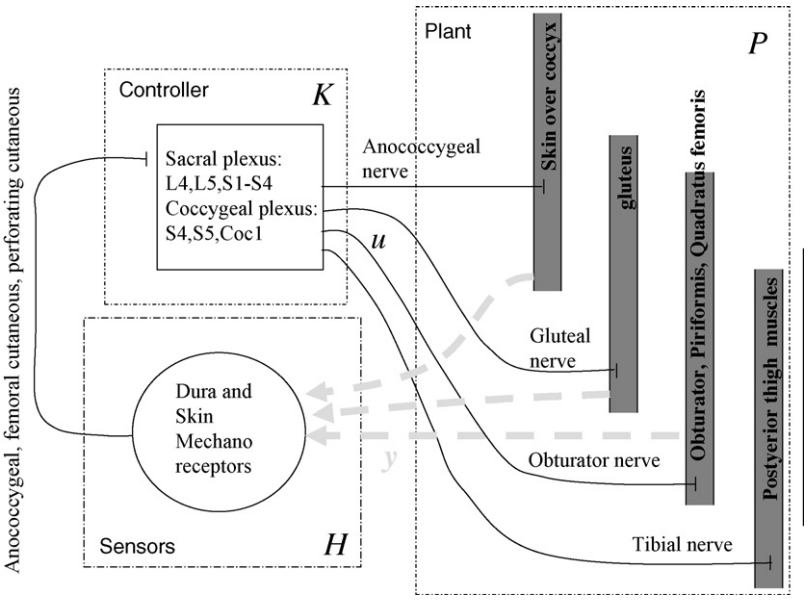

Fig. 8. Sensory-motor loop at sacrum. The hard lines are established pathways, whereas the dotted lines are the conjectured paths through which the loop closes. This diagram is drawn using control conventions: *K* is the controller, *u* is the control action, and *P* is the plant, and *H* is the sensor array.

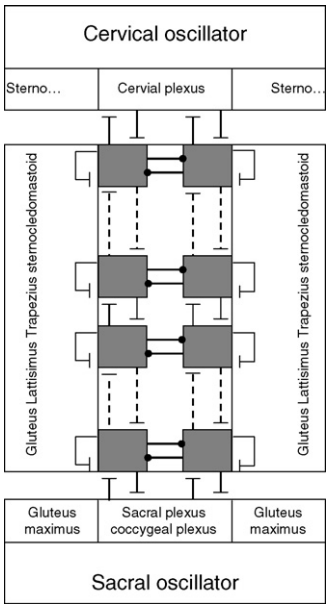

Fig. 9. Overall CPG circuitry extending all along the spine. The diagram is drawn using neurophysiological conventions: Each shaded cell is a bistable oscillator consisting itself of several neurons. There are inhibitory connections between the left and right half centers. The vertical connection are excitatory. The vertical line between the cord and the muscle mass denotes the distributed mechanoreceptors. It is a unique area, the marginal neucleus, in which neurons (in particular α-motoneurons not shown) and mechanoreceptors are congregated [57].

the wave other than by contact at the cervical and sacral areas. This leads us to the conjecture that the neck and sacrum dural vertebral attachment [4] play a crucial role in generating mechanoreceptor signals.

Naturally, for the feedback hypothesis to hold, the bandwidth of the dural mechanoreceptors should be broad enough to allow for the observed D_8 signal.[5] Here, we refer to the experiment of [42, Fig. 1], showing the spike response of mechanoreceptors to unit step pressure stimuli on the dura. From a more quantitative point of view, the shortest latency of the mechanoreceptor response in the tentorium area was estimated to be 27 ms [62, p. 414], which is consistent with the fundamental 13.5 Hz frequency reported in Section 3.1. A related issue depicted in [42, Fig. 1] is the sensitivity of the mechanoreceptors, which respond only above a certain pressure threshold on the dura. It has been consistently observed that the pressure necessary to elicit the oscillation decreases along entrainment, which can be justified by the release of serotonin in the cerebro-spinal fluid [54] along entrainment.[6]

The factorization of the loop function PKH is meant to make the loop fit within the traditional control paradigm, where H, the mechanoreceptors, are the sensors, K, the solar/sacral plexus, is the controller, and P, the innervation of the various muscles, is the plant. In this setup, $u = KHy$, the nerve activity, is the control input. At this stage, it appears difficult to identify P and KH separately, since this would require monitoring the nerve activity u. However, an identification of the composite loop function PKH appears possible. Indeed, the relationship $y = (PKH)y$ indicates that KPH is an operator of which the observed sEMG signal y is a Schauder fixed point.

The conjectured overall circuitry, showing the specific role of the cervical and sacral oscillators, is shown in Fig. 9. This model is based on a chain of bistable oscillators [24,57], with their half centers controlling the opposite motion of the right and left spinal muscles. In a certain sense, it is a bidirectional extension of the model of [24, Fig. 1]. The latter only accommodates for a descending nearest-neighbor excitatory synaptic pathway, while here there is an additional ascending pathway. In another sense, Fig. 9 is a distributed parameter version of the "one CPG per joint" paradigm of [55,38].

This model of course only explains the lateral wave, whereas the longitudinal wave might require other concepts.

5.2. Synchronization of biological oscillators

It is conjectured that the standing wave pattern is the result of the synchronization *at a distance* of the cervical and sacral oscillators. A generic theoretical foundation of synchronization of biological oscillators has been proposed in [52,53]. However, given the rather unique nature of the sacro-cervical synchronization, a more specific synchronization mechanism, based on the network-theoretic concept of incident and reflected waves, was developed in [28]. Spatio-temporal correlation techniques have indeed revealed that, when the wave is still in the traveling mode, traveling bursts reflect on the neck and the sacrum [29].

A related paradigm is the synchronous pattern between the motor nerve firings of the wing and the tail of the marine mollust *Clione* during hunting episodes [40, Figs. 1 and 2]. The connection with the sacro-cervical D_8 coherence can probably be established by performing a wavelet analysis of the signals of [40, Fig. 1].

6. Conclusions

This paper can be looked at either (i) from the viewpoint of standing wave Central Pattern Generator (CPG) or (ii) from the viewpoint of coherence at a significant distance.

From the CPG viewpoint, this paper is an extrapolation of the *traveling wave* CPG concept of [13], inspired from the swimming of the lamprey, to a new *standing wave* CPG concept, better suited for research subjects on the table. Since in both cases this CPG controls many degrees of freedom, at the limit it controls a distributed parameter system, and especially since it involves a traveling wave before synchronization between the distal ends, it is fair to conjecture that this CPG has a circuitry, along with mechanoreceptors, extending all along the spine [57]. The latter is some departure from the other paradigm of simple circuit achieving complex task [18]. The synchronization of the neck and sacral oscillators, concurrent with the standing wave pattern, seems to involve sensory mechanoreceptor input. While the latter might be perceived as a shift from the "no sensory input" paradigm, recent and independent research results [56,38] are already leaning towards a CPG concept that does not require sensory input to develop rhythmic oscillation, but that nevertheless utilizes sensory input for more complicated tasks. Indeed, while there is ample evidence that rhythmic pattern can be generated without sensory input, such a complex behavior as synchronization at a distance seems hard to explain without some sensory input.

The other point of view of coherence at a significant distance is closely related to the first one, as a standing wave along a medium implies coherent motion between the distal ends, with the additional property of 0° or 180° phase locking. Perhaps the most significant contribution of the paper is the confirmation of the statement made in [17] that coordinated motion of different muscles involves EMG coherence at ∼10 Hz. Another somewhat novel feature is that such coherence has been observed over distances significantly larger than those already reported. From a pure signal processing point of view, perhaps another contribution of the paper is the utilization of the DB3 wavelet decomposition in the hunt for

[5] Thanks to Dr. Rolf Johansson, Lund University, for bringing this to our attention.
[6] Thanks to Dr. D. Epstein for this insight.

coherences. As such, instead of asking the question of at *what frequency* the coherence $\hat{\rho}_{ij}(j\omega)$ is maximum as done in [17], here the question has been rephrased as *what subband* of the DB3 wavelet decomposition reveals the best coherence. We also offered a new technique, the "zero crossing nodes," which detects coherence and the stronger standing wave property.

The coherence frequency of ∼12.5–13.5 Hz is at the low end of the β rhythm [36]. This is probably not coincidental, as coherence at that frequency between EMG and EEG signals have been reported [21], but this remains to be investigated further.

The conjectural feedback circuits proposed in Section 5 still need to be positively confirmed. Whether the wave analysis can be used as a tool to asses spinal cord damage and/or recovery [46,59,6] is an issue that is also currently being investigated.

Appendix A. Proofs

Proof of Lemma 1. The function $(f_n \quad g_n) : [0,T] \times [0,L] \to \mathbb{R}^2$ is continuous as an eigenvector of an integral operator with continuous kernel. Indeed, if $(f_n \quad g_n)$ were not continuous, because of the continuity of the kernel of $\begin{pmatrix} 0 & Y^* \\ Y & 0 \end{pmatrix}, \begin{pmatrix} 0 & Y^* \\ Y & 0 \end{pmatrix} \begin{pmatrix} f_n \\ g_n \end{pmatrix}$ would be continuous, contradicting the eigenvector equation. □

Proof of Lemma 2. It suffices to apply the trace theorem to the projection of the operator $\begin{pmatrix} 0 & Y^* \\ Y & 0 \end{pmatrix}$ on its positive spectrum. This projection is clearly $\sum_n \sigma_n \begin{pmatrix} f_n \\ g_n \end{pmatrix} (f_n \quad g_n)$. Then the trace is

$$\sum_n \sigma_n \left(\int_0^T f_n(t) f_n(t)\,\mathrm{d}t + \int_0^L g_n(x) g_n(x)\,\mathrm{d}x \right) = \sum_n \sigma_n$$

The left hand side of the preceding is clearly bounded, so is the right hand side. □

Proof of Theorem 1. It suffices to show that $\{R^N_{x,x'}(s) := \sum_{n,m=1}^N \sigma_n \sigma_m \overline{f_n(t) f_m(t+s)} g_n(x) g_m(x') : N \in \mathbb{N}^*\}$ is a Cauchy sequence for the Hilbert-Schmidt norm [12, XI.6.4]; in other words, $\lim_{N,M\to\infty} ||R^N - R^M||_{HS} = 0$. Specifically,

$$\begin{aligned}
\|R^N - R^M\|^2_{HS} &:= \int\int\int \left(R^N_{x,x'}(s) - R^M_{x,x'}(s)\right)^2 \mathrm{d}x\,\mathrm{d}x'\,\mathrm{d}s \\
&= \int\int\int \left(\sum_{m,n=N}^{M} \sigma_n \sigma_m \overline{f_n(t) f_m(t+s)} g_n(x) g_m(x') \right)^2 \mathrm{d}x\,\mathrm{d}x'\,\mathrm{d}s \\
&= \int\int\int \left(\sum_{n,m,k,l=N}^{M} \sigma_n \sigma_m \sigma_k \sigma_l \overline{f_n(t) f_m(t+s) f_k(t) f_l(t+s)} g_n(x) \right. \\
&\quad \left. \times\ g_m(x') g_k(x) g_l(x') \right) \mathrm{d}x\,\mathrm{d}x'\,\mathrm{d}s \le \frac{1}{T} \int\int \left(\sum_{n,m,k,l=N}^{M} \sigma_n \sigma_m \sigma_k \sigma_l g_n(x) \right. \\
&\quad \left. \times\ g_m(x') g_k(x) g_l(x') \right) \mathrm{d}x\,\mathrm{d}x' = \frac{1}{T} \int\int \left(\sum_{n=N}^{M} \sigma_n g_n(x) \right)^2 \\
&\quad \times \left(\sum_{l=N}^{M} \sigma_l g_l(x') \right)^2 \mathrm{d}x\,\mathrm{d}x'
\end{aligned}$$

and convergence follows from the trace class property. □

References

[1] D.E. Amundsen, M.P. Mortell, T.A. Cox, Standing wave solutions of periodically forced kdv equations, in: Fourth International Conference on Dynamic Systems and Applications, Department of Mathematics, Morehouse College, Atlanta, GA, USA, 2003.

[2] A. Bibbig, R.D. Traub, M.A. Whittington, Long range synchronization of γ and β oscillations and the plasticity of excitatory and inhibitory synapses: a network model, Journal of Neurophysiology 88 (2002) 1634–1654.

[3] S. Bohacek, E.A. Jonckheere, Chaotic modeling in network spinal analysis: Preliminary report: nonlinear canonical correlation with alternating conditional expectation (ACE), Journal of Vertebral Subluxation Research 2 (December(4)) (1998) 188–195.

[4] A. Breig, Adverse Mechanical Tension in the Central Nervous System, John Wiley and Sons, New York, 1987.

[5] M.G. Bulmer, Principles of Statistics, Dover, New York, 1979.

[6] G. Courtine, B. Song, R.R. Roy, H. Zhong, J.E. Herrmann, Y. Ao, J. Qi, V.R. Edgerton, M.V. Sofroniew, Recovery of supraspinal control of stepping via indirect propriospinal relay connections after spinal cord injury, Nature Medicine 14 (1) (2008) 69–74.

[7] I. Daubechies, Orthonormal bases of compactly supported wavelets, Communications on Pure and Applied Mathematics XLI (1988) 909–996.

[8] I. Daubechies, Ten lectures on wavelets, in: CBMS-NSF Conference Series in Applied Mathematics, SIAM, 1992.

[9] S. Day, Important factors in surface EMG measurement, Technical Report, Bortec Biomedical Ltd., 225, 604-1st St. Sw, Calgary, AB, T2P 1M7, Canada, 2000.

[10] S.J. Day, M. Hulliger, Experimental simulation of cat electromyogram: Evidence for algebraic summation of motor-unit action-potential trains, The Journal of Neurophysiology 86 (November(5)) (2001) 2144–2158.

[11] M.R. Dimitrijevic, Y. Gerasimenko, M.M. Pinter, Evidence for a spinal Central Pattern Generator in humans, Neuronal Mechanisms for Generating Locomotor Activity; Annals New York Academy of Sciences 38 (1998) 360–376.

[12] N. Dunford, J.T. Schwartz, Linear Operators. Part II. Spectral Theory, Self-Adjoint Operators in Hilbert Spaces, Wiley Classics, Wiley, New York, 1963.

[13] C. Eliasmith, C.H. Anderson, Rethinking Central Pattern Generators: a general approach, Neurocomputing 32–33 (1–4) (2000) 735–740.

[14] G.B. Ermentrout, N. Kopell, Fine structure of neural spiking and synchronization in the presence of conduction delays, Proceedings of the National Academy of Sciences of United States of America 95 (February) (1998) 1259–1264.

[15] F. Ascani, et al., Detection of low-dimensional chaos in quasi-periodic time series: the 0–1 test, Technical Report, Santa Fe Institute Complex Systems Summer School, 2008.

[16] S.F. Farmer, et al., Changes in EMG coherence between long and short thumb abductor muscles during human development, Journal of Physiology 579 (2) (2007) 389–402.

[17] S.F. Farmer, Rhythmicity, synchronization and binding in human and primate motor systems, Journal of Physiology 509 (1) (1998) 3–14.

[18] W. Frost, P. Katz, Single neuron control over a complex motor program, Proceedings of the National Academy of Sciences of United States of America 93 (January) (1996) 422–426.

[19] M. Grattarola, M. Ciappalone, F. Davide, S. Martinoira, M.B. Tedesco, N. Rosso, A. Vato, Burst analysis of chemically stimulated spinal cord neuronal networks cultured on microelectrode arrays, Technical Report, Neural and Bioelectronic Technologies group, Department of Biophysical and Electronic Engineering, University of Genoa, Italy, 2004.

[20] S. Grillner, P. Wallén, Central Pattern Generators for locomotion, with special reference to vertebrates, Annual Review of Neuroscience 8 (1985) 233–261.

[21] D.M. Halliday, B.A. Conway, S.F. Farmer, J.R. Rosenberg, Using electroencephalography to study functional coupling between cortical activity and electromyograms during voluntary contractions in humans, Neuroscience Letters 241 (1998) 5–8.

[22] T. Heimburg, A.D. Jackson, On soliton propagation in biomembranes and nerves, Proceedings of the National Academy of Sciences of United states of America 102 (July(28)) (2005) 9790–9795.

[23] A. Hiebert, E. Jonckheere, P. Lohsoonthorn, V. Mahajan, S. Musuvathy, M. Stefanovic, Visualization of a stationary CPG-revealing spinal wave, in: J.D. Westwood, et al. (Eds.), Medicine Meets Virtual Reality 14: Accelerating Change in Healthcare: Next Medical Toolkit, Technology and Informatics, IOS Press, Amsterdam/Berlin/Oxford/Tokyo/Washington, D.C., 2006. Available at: http://eudoxus.usc.edu/CHAOS/nsa.html.

[24] S.A. Hill, X.-P. Liu, M.A. Borla, J.V. José, D.M. O'Malley, Neurokinematic modeling of complex swimming patterns of the larval zebrafish, Neurocomputing 65–66 (June) (2005) 61–68.

[25] A.J. Ijspeert, A connectionist central pattern generator for the terrestrial and aquatic gaits of a simulated salamander, Biological Cybernetics 84 (2001) 331–348.

[26] A.J. Ijspeert, Locomotion, vertebrate, in: M. Arbib (Ed.), The Handbook of Brain Theory and Neural Networks, 2nd ed., MIT Press, Cambridge, MA, 2002.

[27] D. Jacobs, B. Mckinney, M. Shearer, Traveling wave solutions of the modified Korteweg-deVries-Burgers equation, Journal of Differential Equations 116 (March(2)) (1995) 448–467.

[28] E. Jonckheere, S. Musuvathy, M. Stefanovic, A biologically inspired synchronization of lumped parameter oscillators through a distributed parameter channel, in: IFAC Workshop on Control of Distributed Parameter Systems (CDPS), University of Namur (FUNDP), Namur, Belgium, July 2007. http://www.fundp.ac.be/sciences/cdps07/.

[29] E.A. Jonckheere, P. Lohsoonthorn, Spatio-temporal analysis of an electrophysiological wave phenomenon, in: International Symposium on the Mathematical Theory of Network and Systems (MTNS2004), Leuven, Belgium, 2004. Available at: http://eudoxus.usc.edu/CHAOS/nsa.html.
[30] E.A. Jonckheere, P. Lohsoonthorn, R. Boone, Dynamic modeling of spinal electromyographic activity during various conditions, in: Proceeding of the American Control Conference, Denver, CO, June 4–6, 2003, pp. 465–470. Biomedical Applications Session. Available at: http://eudoxus.usc.edu/CHAOS/nsa.html.
[31] E.A. Jonckheere, P. Lohsoonthorn, V. Mahajan, Chirosensor–an array of non-invasive sEMG electrodes, in: J.D. Westwood, et al. (Eds.), Medicine Meets Virtual Reality 13: The Magical Next Becomes the Medical Now, volume 111 of Technology and Informatics, IOS Press, Amsterdam/Berlin/Oxford/Tokyo/Washington, D.C., 2005, pp. 234–236. Available at: http://eudoxus.usc.edu/CHAOS/nsa.html.
[32] E.N. Kamavuakoa, D. Farina, Estimation of muscle fiber conduction velocity of doublet discharges, Biomedical Signal Processing and Control 2 (October(4)) (2007) 331–338.
[33] J.M. Kilner, R.J. Fisher, R.N. Lemon, The coupling of oscillatory activity between muscles is strikingly reduced in a deafferented subject compared with normal controls, Journal of Neurophysiology 92 (April) (2004) 790–796.
[34] D. Kleinfeld, R.W. Berg, S.M. O'Connor, Anatomical loops and their electrical dynamics in relation to whisking by rat, Somatosensory & Motor Research 16 (2) (1999) 69–88.
[35] N. Kopell, We got rhythm: dynamical systems of the nervous system, Notice of the AMS 47 (January(1)) (2000) 6–16.
[36] N. Kopell, G.B. Ermentrout, M.A. Whittington, R.D. Traub, Gamma rhythms and beta rhythms have different synchronization properties, Proceedings of the National Academy of Sciences of United States of America 97 (February(4)) (2000) 1867–1872.
[37] C.S. Kubrusly, N. Levan, Shift reducing subspaces and irreducible-invariant subspaces generated by wandering vectors and applications, Mathematics and Computers in Simulation 65 (6) (2004) 607–627.
[38] A.D. Kuo, The relative roles of the feedforward and feedback in the control of rhythmic movements, Motor Control 6 (2002) 129–145.
[39] N. Levan, C.S. Kubrusly, A wavelet "time-shift-detail" decomposition, Mathematics and Computers in Simulation 63 (2) (2003) 73–78.
[40] R. Levi, P. Varona, Y.I. Arshavsky, M.I. Rabinovich, A.I. Selverston I, The role of sensory network dynamics in generating a motor program, The Journal of Neuroscience 25 (October(42)) (2005) 9807–9815, doi:10.1523/JNEUROSCI.2249-05.2005.
[41] D. Levy, A. Strassman, Mechanical response properties of A and C primary afferent neurons innervating the rat intracranial dura, Journal of Neurophysiology 88 (2002) 3021–3031.
[42] D. Levy, A.M. Strassman, Mechanical response properties of A and C primary afferent neurons innervating the rat intracranial dura, Journal of Neurophysiology 88 (December) (2002) 3021–3031, doi:10.1152/jn.00029.2002.
[43] P. Lohsoonthorn, E. Jonckheere, Nonlinear switching dynamics in surface electromyography of the spine, in: Conference on Physics and Control, St. Petersbourg, Russia, 2003, pp. 277–282. Available at: http://eudoxus.usc.edu/CHAOS/nsa.html.
[44] C.J. De Luca, A. Adam, Decomposition and analysis of intramuscular electromyographic signals, in: U. Windhorst, H. Johansson (Eds.), Modern Techniques in Neuroscience Research, Springer, Heidelberg, 1999, pp. 757–776 (Chapter 27).
[45] A.D. McClellan, W. Jang, Mechanosensory input to the central pattern generator for locomotion in the lamprey spinal cord: resetting, entrainment, and computer modeling, Journal of Neurophysiology 70 (December(6)) (1993) 2442–2454.
[46] J.W. McDonald, D. Becker, C. Sadowsky, J.A. Jane, T.E. Conturo, L. Schultz, Late recovery following spinal cord injury, Journal of Neurosurgery (Spine 2) 97 (2002) 252–265.
[47] B.R. Moon, Sampling rates, aliaising, and the analysis of electrophysiological signals, in: P.K. Bajpai (Ed.), Proc. of the 15th Southern Biomedical Engineering Conference, IEEE, Piscataway, NJ, 1966, pp. 401–404.
[48] S. Musuvathy, E. Jonckheere, Evidence of spatio-temporal transition to chaos in the spine, in: 4th International Symposium on Communications, Control, and Signal Processing, Limassol, Cyprus, March, 2010.
[49] K. Nakada, T. Asai, H. Hayashi, Burst synchronization in two pulse-coupled resonant-and-fire neuron circuits, vol. 218/2006, Springer, Boston, 2006, pp. 285–294. http://pitagoras.usach.cl/gfelipe/wcc/papers/Symposium/Article_30-Nakada.pdf.
[50] O. Haug Olsen, D. Murray-Smith, Quantifying periodic activity in central pattern generators: the crayfish swimmeret, Journal of Neuroscience Methods 50 (1993) 25–35.
[51] C.S. Ong, X. Mary, S. Canu, A.J. Smola, Learning with non-positive kernels, in: Proceedings 21st International Conference on Machine Learning, Banff, Canada, 2004.
[52] V. Paar, N. Pavin, M. Rosandic, Energy dependence of self-similarity truncation in a system of weakly coupled dissipative oscillators relevant for biological systems, Fizika A 10 (3) (2001) 95–104.
[53] V. Paar, N. Pavin, M. Rosandic, Link between truncated fractals and coupled oscillators in biological systems, Journal of Theoretical Biology 212 (2) (2001) 47–56.
[54] V.M. Pastor, D.L. MacMillan, The action of proctolin, octopamine and serotonin on crustacean proprioceptors show species and neurone specificity, Journal of Experimental Biology 152 (1990) 485–504.
[55] C. Paul, M. Bellotti, S. Jezernik, A. Curt, Development of a human neuromusculo-skeletal model for investigation of spinal cord injury, Biological Cybernetics 93 (2005) 153–170.
[56] K.G. Pearson, J.M. Ramirez, Sensory modulation of pattern generating circuits, in: P.S.G. Stein, S. Grillner, A. Selverstonand, D.G. Stuart (Eds.), Neurons, Network, and Motor Behavior, MIT Press, Cambridge, 1997, pp. 225–236.
[57] D.M. Schroeder, The marginal nuclei in the spinal cord of reptiles: intraspinal mechanoreceptors, Ohio Journal of Science 86 (3) (1986) 69–72.
[58] E.E. Selkurt, Physiology, Little, Brown and Company, Boston, 1971.
[59] R. Shalaby, T. Schauer, H. Nahrstaedt, J. Raisch, Voluntary muscle activity detection using a single pair of electrodes for EMG controlled FES, pp. 69–71, in: Proc. of the 14th Annual Conference of the International Functional Electrical Stimulation Society (IFESS 2009), Seoul, Korea, September, 2009.
[60] W.M. Sloboda, V.M. Zatsiorsky, Wavelet analysis of EMG signals, in: Twenty-First Annual Meeting of the American Society of Biomechanics, Clemson University, South Carolina, September 24–27, 1997.
[61] G. Strang, T. Nguyen, Wavelets and Filter Banks, Wellesley, Cambridge, 1996.
[62] A.M. Strassman, S.A. Raymond, Electrophysiological evidence for tetrodotoxin-resistant sodium channels in slowly conducting dural sensory fibers, Journal of Neurophysiology 81 (1999) 413–424.
[63] R. Warick, P.L. Williams (Eds.), Gray's Anatomy, 35th British ed., W.B. Saunders Co., Philadelphia, 1973.